CELL MEMBRANES SUSTAIN PHOSPHOLIPID IMBALANCE VIA CHOLESTEROL ASYMMETRY

Milka Doktorova[1*+], Jessica L. Symons[2*], Xiaoxuan Zhang[1], Hong-Yin Wang[1], Jan Schlegel[3], Joseph H. Lorent[4], Frederick A. Heberle[5], Erdinć Sezgin[3], Edward Lyman[6], Kandice R. Levental[1+], Ilya Levental[1+]

[1] Department of Molecular Physiology and Biological Physics, University of Virginia, Charlottesville, VA 22903, USA;
[2] Department of Integrative Biology & Pharmacology, University of Texas Health Science Center at Houston, Houston, TX 77030, USA;
[3] Science for Life Laboratory, Department of Women's and Children's Health, Karolinska Institutet, 17165 Solna, Sweden;
[4] Department of Cellular and Molecular Pharmacology, TFAR, LDRI, UCLouvain, Avenue Mounier 73, B1.73.05, B-1200 Brussels;
[5] Department of Chemistry, University of Tennessee Knoxville, Knoxville, TN 37916, USA;
[6] Department of Physics and Astronomy; Department of Chemistry and Biochemistry, University of Delaware, Newark, DE 19716, USA

* These authors contributed equally to this work.
[+] Co-corresponding authors: md4xm@virginia.edu, krl6c@virginia.edu, il2sy@virginia.edu

ABSTRACT

Membranes are molecular interfaces that insulate cells from external stresses, compartmentalize the cytoplasm, and control the flow of nutrients and information[1]. These functions are facilitated by diverse collections of lipids, nearly all of which are distributed asymmetrically between the two leaflets of living bilayers[2,3]. Previous models of biomembrane structure and function have rested upon the implicit assumption that the two membrane leaflets have similar abundances of phospholipids. Here, we show that this assumption is generally invalid and investigate the consequences of lipid abundance imbalances in mammalian plasma membranes (PM). Using quantitative lipidomics, we discovered that cytoplasmic leaflets of human erythrocyte PMs have >50% overabundance of phospholipids compared to exoplasmic leaflets. We show that this phospholipid imbalance is enabled by an asymmetric interleaflet distribution of cholesterol[4,5], which rapidly redistributes to buffer leaflet stresses. Asymmetric phospholipid abundance and composition combine to enrich cholesterol in the exoplasmic PM leaflet. Through a combination of experimental and computational approaches we demonstrate how these lipid distributions impart unique functional characteristics to PMs, including low permeability, surprisingly fast cholesterol diffusion[6], and resting tension in the cytoplasmic monolayer that regulates protein localization. Our observations of these previously overlooked aspects of membrane asymmetry represent an evolution of classic paradigms[1,7] of biomembrane structure and physiology.

Introduction

The plethora of molecular processes at the cellular plasma membrane (PM) is enabled by a diverse set of membrane proteins, but also by the membrane's lipid matrix. One characteristic feature of eukaryotic PMs is their compositional asymmetry, i.e. drastically different phospholipid (PL) compositions of the two bilayer leaflets[3,8,9]. This asymmetry is established and maintained by ATP-driven enzymes that directionally flip PLs across the bilayer[10,11]. These regulated processes produce leaflets with distinct compositions and physical properties, including relatively tightly packed exoplasmic leaflets and more charged and fluid cytoplasmic leaflets[2]. The interleaflet distribution of cholesterol, a major PM component, remains elusive amid conflicting reports[4]. While specific lipid compositions differ between organisms and cell types, structural features of protein transmembrane domains shared across various organisms suggest that most eukaryote PMs are asymmetric[2].

PM asymmetry has been associated with many cellular functions, most notably apoptosis, wherein cell surface exposure of the cytoplasmic leaflet lipid phosphatidylserine (PS) is a central hallmark[10]. PS exposure on platelets is also required for activation of blood coagulation enzymes[11]. This release of lipid asymmetry is often referred to as 'scrambling' and is mediated by ATP-independent lipid channels[11]. More recently, PM asymmetry has been implicated in cell-cell fusion[12], viral entry[13], and intracellular signaling[14]; however, in most cases, it is not lipid asymmetry *per se*, but rather its loss that is associated with cellular responses[15,16]. Thus, despite accumulating evidence for the prominent chemical and physical asymmetries of PM bilayers, it is yet unknown why most cells expend significant metabolic resources to maintain steady-state membrane lipid distributions far away from their symmetric equilibrium.

Here, integrating cellular, biochemical, and computational approaches, we report the discovery of a previously overlooked aspect of membrane asymmetry central to the structure and function of mammalian PMs: namely, large PL abundance imbalances between PM leaflets. Such imbalances are enabled by highly asymmetric distributions of cholesterol, which can rapidly redistribute to buffer leaflet imbalances. These unexpected phospholipid and cholesterol distributions produce unique membrane properties that reveal novel functional roles for steady-state PM asymmetry and its regulated release. The abundance imbalance of major lipid constituents thus represents a novel dimension of functional membrane organization.

Lipid imbalance in plasma membranes

Recently, we combined enzymatic digestion of exoplasmic leaflet lipids with shotgun mass spectrometry to quantify the molecularly detailed compositional asymmetry of nearly all PL classes in the human erythrocyte PM[2]. Here, we completed the characterization of the known erythrocyte PM lipidome by quantifying glycosphingolipids (GSLs) and cholesterol abundances. We found that GSLs constitute ~15 mol% of exoplasmic leaflet lipids (Figures 1A, S1B) while cholesterol is present at 40 (± 1) mol% of PM lipids (Figure 1C). Due to its rapid transbilayer diffusion, cholesterol's interleaflet distribution is not accessible by enzymatic approaches[4].

Internal standards in mass spectrometry measurements allow absolute quantification of individual lipid species, which can then be used to compare total PL abundances between the two PM leaflets. Surprisingly, we found that the cytoplasmic leaflet has 1.5–2.3-fold more phospholipids than the exoplasmic leaflet (Figure 1B) (for simplicity, 'PLs' here includes GSLs despite their not having a phosphate group). Such a large difference in PL abundances between leaflets was unexpected because monolayer areas in a bilayer must match. This imbalance cannot be explained by membrane components not included in this analysis, such as GPI-anchored proteins, phosphoinositides, or protein transmembrane domains (see SI text, section 2.5 for discussion). Notably, differences in interleaflet PL abundances are not unprecedented, with similar imbalances evident when the foundational data that originally reported lipid asymmetry[3,17-20] is reanalyzed (Figure 1D and Table S1).

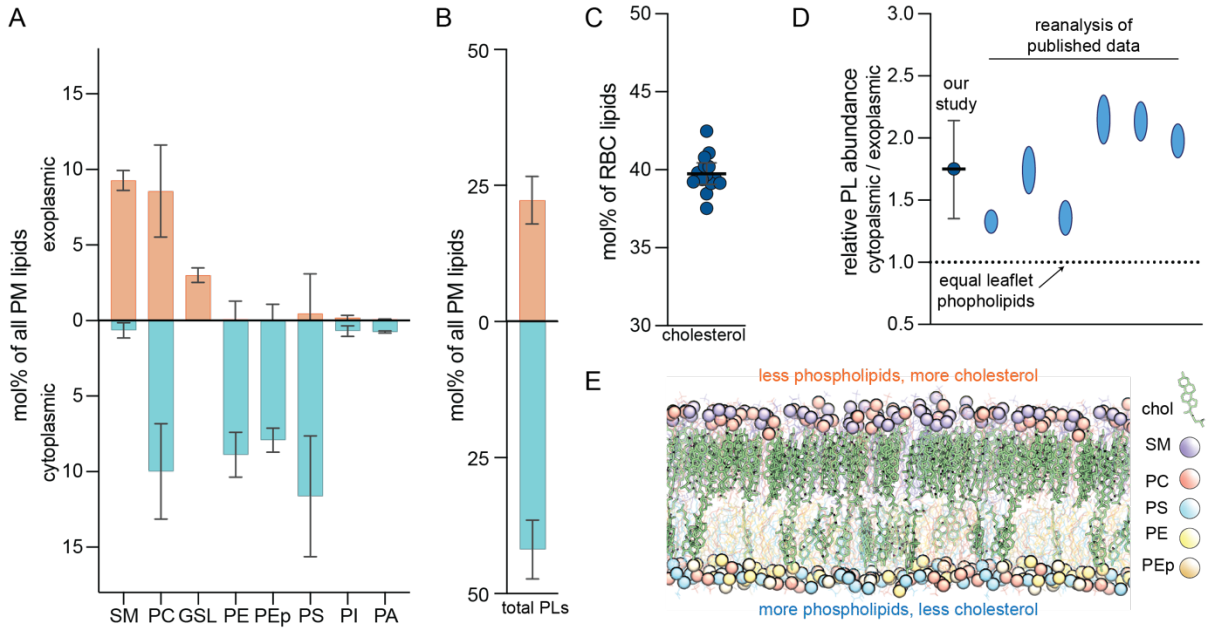

Figure 1 | The exoplasmic leaflet of erythrocyte PMs has fewer phospholipids. a, Shotgun mass spectrometry quantifications of asymmetric distribution of various lipid classes in the erythrocyte PM. Exoplasmic and cytoplasmic lipidomes are determined by phospholipase treatment of live cells and include species with a variety of chain compositions. Values represent mol% of lipid class as a percentage of PM lipids, with interleaflet distribution shown in orange/blue bars. Average +/- st.dev. from >3 independent experiments. SM sphingomyelin, PC phosphatidylcholine, GSL glycosphingolipids, PE phosphatidylethanolamine, PEp PE plasmalogen, PS phosphatidylserine, PI phosphatidylinositol, PA phosphatidic acid. **b,** Total phospholipid (including GSLs) abundances of the two PM leaflets obtained by summing the corresponding leaflet components in **a**. **c,** Cholesterol measured by lipidomics as a mol% of all erythrocyte lipids. The mean is 40 (± 1) mol% of PM lipids, however its transbilayer distribution cannot be resolved by this analysis. Data comes from untreated erythrocyte samples from different experiments which were corrected for the presence of GSLs. **d,** Relative total phospholipid (PL) abundances between the two PM leaflets of erythrocytes from this work and from re-analysis of previous reports (Table S1). **e,** Snapshot of an equilibrated atomistic computational model of the erythrocyte PM with overabundance of PLs in the cytoplasmic leaflet (Cyto+ model, Table S5). The membrane contains 40 mol% cholesterol, which converges to an asymmetric distribution with ~3-fold enrichment in the exoplasmic leaflet. Lipid classes are color-coded (phosphorous atoms shown as spheres; cholesterol in green). Structures of major PLs identified in **a** and used in simulations shown in Figure S2.

Phospholipid imbalance is sustained by cholesterol

To investigate the previously dismissed[19] feasibility of a membrane with extensive PL abundance imbalance, we built an atomically detailed computational PM model with lipid compositions of the two leaflets guided by lipidomics data (Table S5). The model was built with more phospholipids in the cytoplasmic leaflet (relative to the exoplasmic one) and was termed Cyto+ (Figure 1E). The simulated Cyto+ membrane also contained 40 mol% cholesterol, with initial interleaflet distribution adjusted to ensure matching leaflet surface areas. Having the unique ability to quickly flip-flop between leaflets[21,22], cholesterol equilibrated its distribution during the 17 μs-long trajectory, with 77% of cholesterol molecules accumulating in the PL-poor exoplasmic leaflet (Figure 1E). Thus, we hypothesized that cholesterol can enrich in PL-poor leaflets, enabling large interleaflet phospholipid imbalances.

To test this hypothesis, we simulated a series of coarse-grained asymmetric bilayers with fixed PL leaflet imbalance (cytoplasmic leaflet having 35% more PLs than exoplasmic) and cholesterol abundances ranging from 10 to 50 mol% (Figure 2A, Table S2). In all these simulations, cholesterol equilibrated to an asymmetric distribution, accumulating in the exoplasmic, PL-poor leaflet (Figure S3). Notably, low cholesterol concentrations were unable to sustain stable, flat bilayer morphologies; instead, the systems adopted unusual, nonlamellar configurations (Figure 2A). In contrast, membranes with ≥30 mol%

cholesterol produced stable, flat bilayers, confirming that cholesterol (in sufficient abundance) enables tolerance for large PL imbalances via its asymmetric interleaflet distribution.

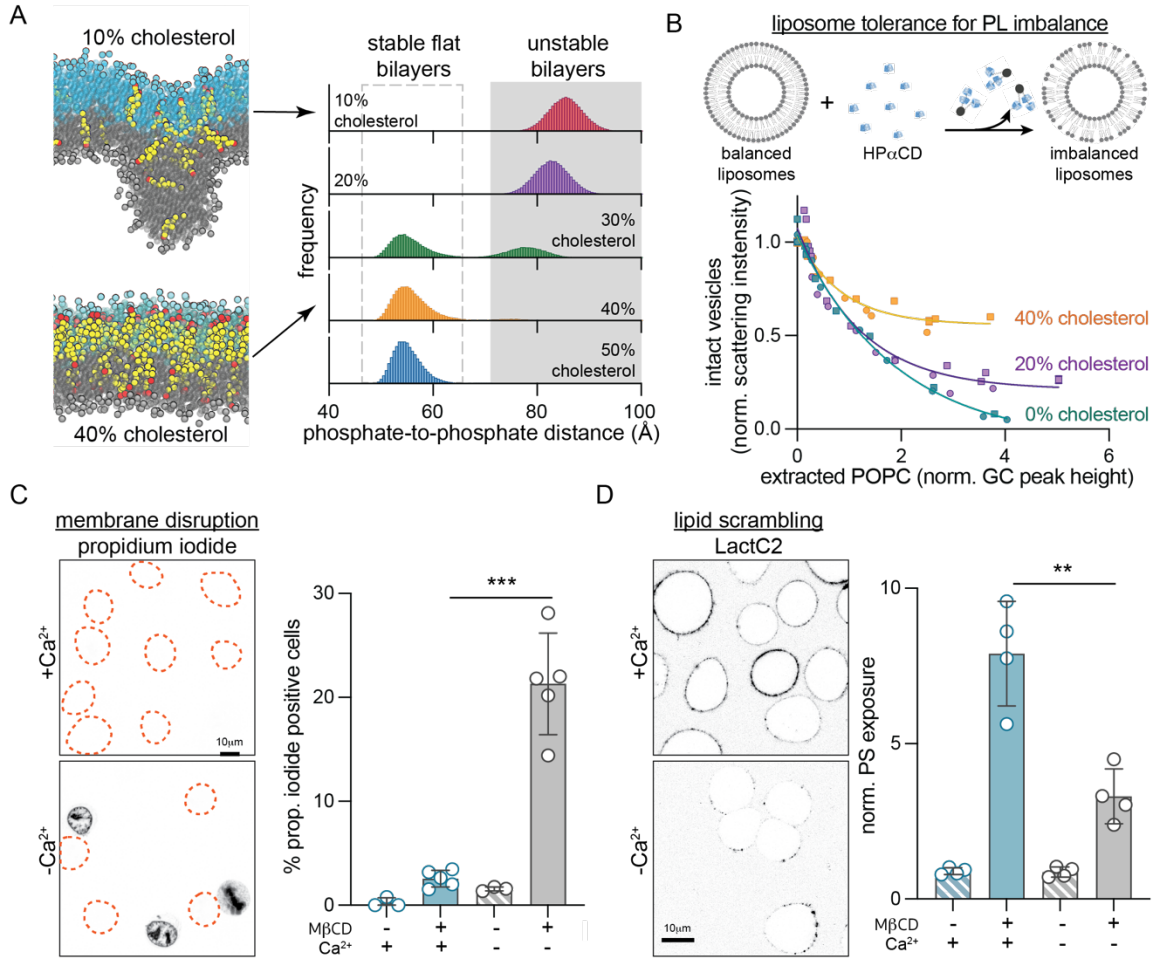

Figure 2 | Cholesterol imparts tolerance for phospholipid abundance imbalance between membrane leaflets. a, Coarse-grained simulations of a PM model with 35% more PLs in the cytoplasmic leaflet and varying cholesterol abundance (10-50%, Table S2). Histograms show the distributions of maximal distances between lipid phosphate groups in the two leaflets. Values >70 Å indicate unstable bilayers with non-lamellar morphology. Representative snapshots from simulated bilayers with 10 and 40% cholesterol shown for reference (exoplasmic leaflet PL phosphate groups shown in cyan, cytoplasmic in gray, cholesterol is yellow with hydroxyl headgroup in red). **b,** Extraction of external leaflet PLs from extruded liposomes with 0, 20 and 40 mol% cholesterol. POPC is extracted from the external leaflet by HPαCD, which induces PL imbalance between leaflets causing membrane instability and liposome destruction. Amount of extracted lipid is quantified by GC/MS, while the corresponding fraction of intact vesicles is measured by light scattering (data from two independent experiments). **c,** Extraction of cholesterol compromises PM integrity if lipid scrambling is suppressed using Ca^{2+}-free media, evidenced by propidium iodide (PI) staining of nuclei. Outlines represent PI-negative cells. **d,** Extraction of cholesterol from the PM of RBL cells with MβCD leads to scrambling of PM lipids evidenced by exposure of PS on the cell surface (binding of external PS-marker, LactC2-mClover), while suppressing scrambling reduces PS exposure. Average intensity of LactC2-mClover on the PM (PS exposure) normalized to −MβCD is shown on the right. Data shown in **c** and **d** is from 3–5 independent experiments.

To experimentally evaluate this inference, we measured the tolerance of liposomes to PL imbalance via single-sided lipid extraction (Figure 2B). Large unilamellar vesicles (composed of POPC with 0-40 mol% cholesterol) were titrated with 2-hydroxypropyl-α-cyclodextrin (HPαCD), a cyclic polysaccharide that avidly extracts PLs but not cholesterol from the outward-facing membrane leaflet[23]. More HPαCD extracts more PL, inducing larger leaflet imbalances, which ultimately destroy the liposomes, evidenced by decreased light scattering (Figure S4). By directly quantifying the amount of extracted POPC (i.e. induced

interleaflet PL abundance imbalance) by gas chromatography, we observed that cholesterol protects vesicles from destruction in a dose-dependent fashion, consistent with simulations (Figure 2B).

We measured that cholesterol comprises ~40 mol% of PM lipids in erythrocytes, consistent with previous estimates in mammalian PMs[4]. Our simulations and synthetic membrane experiments suggest that such high cholesterol levels are required to sustain large PL imbalances (Figure 2A–B). Thus, we hypothesized that extracting cholesterol from cell PMs would destabilize the bilayer and compromise membrane integrity. We selectively extracted cholesterol from the PM of cultured rat basophil leukemia (RBL) cells with methyl-β-cyclodextrin (MβCD), which depletes both PM leaflets due to cholesterol's rapid transbilayer movement[24] but does not extract PLs[25]. Contrary to our prediction, membrane integrity was not affected by MβCD, as revealed by lack of propidium iodide (PI) staining (Figure 2C) or permeability to dextran polymers (Figure S5, top). Rather, as previously reported in erythrocytes[26], cholesterol extraction induced rapid PL scrambling evidenced by externalization of inner-leaflet PS (Figure 2D, S5A), which would likely eliminate any pre-existing PL imbalance between leaflets. To suppress scrambling and thereby isolate the effects of PL imbalance, we relied on the calcium dependence of the most widely characterized scramblase TMEM16F[11]. Indeed, treatment of RBL cells with MβCD in a Ca^{2+}-free buffer significantly reduced PS exposure (Figure 2D, S5A). Strikingly, this treatment also disrupted membrane integrity, revealed by robust staining of nuclei with PI (Figure 2C, S5B) and leakage of dextran into the cytoplasm (Figure S5C). These results reveal that in response to cholesterol extraction, PLs redistribute between PM leaflets to preserve membrane integrity. If this mechanism is inhibited, membrane integrity is lost, supporting the notion that cholesterol imparts tolerance for interleaflet PL abundance imbalance in living cells.

Cholesterol distribution in the PM

Our asymmetric Cyto+ model indicates that cholesterol can balance excess PLs in the cytoplasmic leaflet by accumulating in the exoplasmic leaflet (Figure 1E). PL imbalance in the PM can be established by the activity of enzymes termed flippases, which use ATP to translocate aminophospholipids (e.g. PS) from the exoplasmic to the cytosolic leaflet against their concentration gradient[11]. In the absence of compensatory lipid movement to the exoplasmic leaflet, such active lipid flipping can over-populate the inner leaflet, creating tension in the under-populated leaflet and compression in the over-populated one. This effect was confirmed by a series of simulations in which increasing numbers of PS lipids were flipped into the 'inner' leaflet (Figure 3A). We also found that the resulting stresses could be alleviated by cholesterol spontaneously 'flopping' to the outer leaflet, consistent with previous reports of rapidly flipping lipids buffering leaflet tension[22,27] (Figure 3A).

In addition to this stress-buffering role, cholesterol preferentially interacts with saturated versus unsaturated lipids[28]. To incorporate this effect, we simulated a series of coarse-grained asymmetric membranes with one fully saturated (outer) and one highly unsaturated (inner) leaflet. Interleaflet PL abundances were varied, while cholesterol was initiated at 30 mol% in both leaflets (Figure 3B). In nearly all cases, we observed net cholesterol flux towards the outer leaflet (Figure 3B); e.g. when PLs were initially balanced, cholesterol equilibrates at >40 mol% in the outer leaflet (~4-fold enriched relative to unsaturated leaflet) producing an over-populated outer leaflet even at the cost of generating, rather than alleviating, membrane stress (Figure S6). Net cholesterol flux could only be eliminated when the outer leaflet had 2-fold more PLs than the inner.

These findings reveal that cholesterol's preference for certain lipid classes (saturated lipids, sphingolipids) combines with its tendency to populate under-packed leaflets to determine its ultimate transbilayer distribution[5,29]. In our lipidomics measurements, erythrocyte PM exoplasmic leaflets are more saturated (Figure S1A), rich in sphingolipids (Figure 1A), and PL-underpopulated (Figure 1B), making a strong prediction for cholesterol enrichment therein.

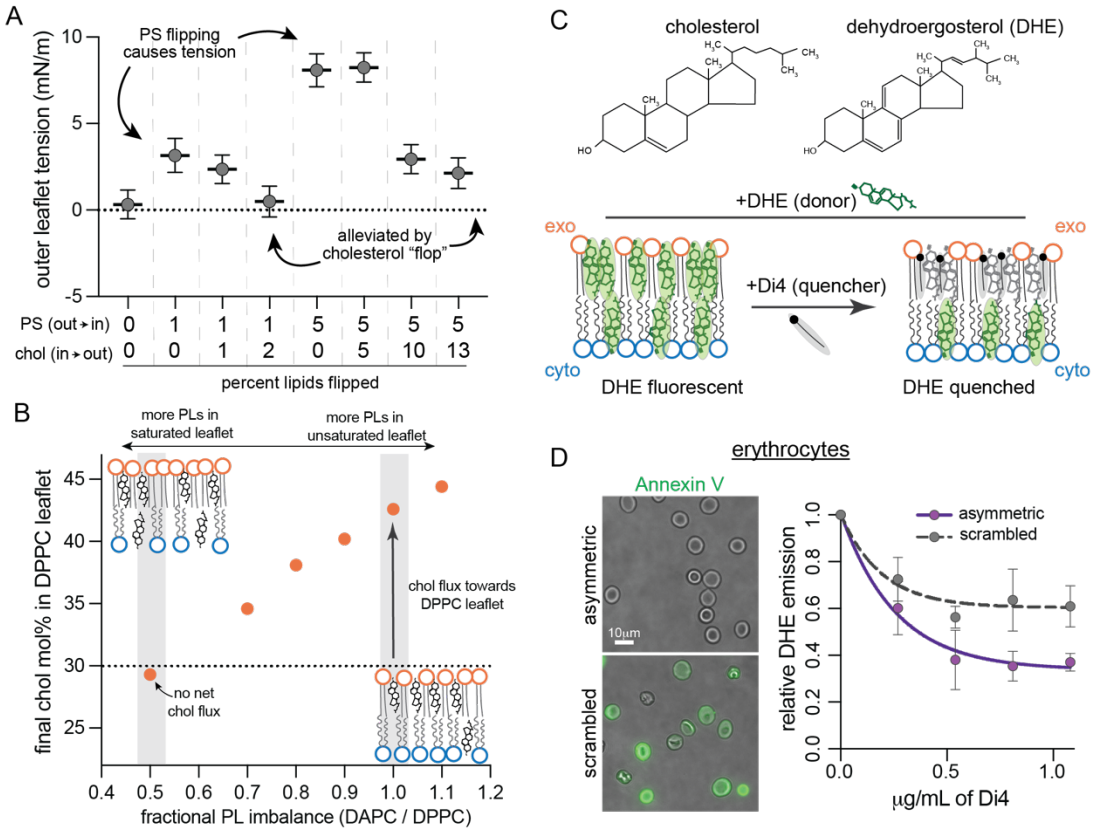

Figure 3 | Cholesterol interleaflet distribution in model and cell membranes. a, Leaflet tension (differential stress) in the outer leaflet of simulated bilayers composed of POPS (PS), POPC and cholesterol (Chol) modeling different extents of PS and Chol flipping. Atomistic bilayers were constructed with the indicated percentage of PS lipids effectively fl**i**pped from the outer leaflet to the inner leaflet, and Chol molecules fl**o**pped from the inner to the outer leaflet (Table S3). Leaflet tension was calculated from equilibrated lateral pressure distributions. **b,** Cholesterol distribution in coarse-grained asymmetric bilayers composed of a fully saturated outer leaflet (DPPC) with fixed number of PLs opposing a highly unsaturated inner leaflet (DAPC) with varying PL abundance (Table S4). The fractional imbalance of DAPC-to-DPPC lipids goes from underpopulated DAPC leaflet (left) to underpopulated DPPC leaflet (right). Chol was initiated at 30 mol% in each leaflet. Simulations were run for 10 μs allowing Chol to equilibrate between the two leaflets; the equilibrated cholesterol concentrations in the outer leaflet are plotted. Schematics of the equilibrated relative lipid distributions are shown for comparison. **c,** Schematic illustration of the experimental setup for measuring Chol interleaflet distribution in erythrocytes. Small fraction (<10%) of cholesterol in the erythrocyte PM is exchanged with DHE. A quencher, Di4, is added exogenously and resides exclusively in the outer leaflet. The fraction of DHE fluorescence quenched by Di4 provides a readout of the relative amount of DHE in the exoplasmic leaflet. **d,** DHE fluorescence in erythrocyte membranes as a function of increasing Di4 concentration. Data shown for untreated cells and cells whose PM lipids were scrambled with 100 μM PMA. Representative images show binding of PS-marker Annexin V before (top) and after (bottom) PMA treatment. Avg +/- st.dev. for 3 independent experiments.

To test this prediction, we developed an assay to measure cholesterol distribution in a living cell PM. Erythrocytes were isolated from healthy donors and a small fraction of cholesterol was exchanged for the fluorescent cholesterol analog, dehydroergosterol (DHE, Figure 3C), which has similar chemical and biophysical properties[30,31]. We assayed the asymmetric distribution of DHE by fluorescence resonance energy transfer (FRET) to a quencher present only in the outer leaflet (Figure 3C). To that end, we added the fluorophore Di4 (which is charged and cannot flip between leaflets[2]) into the erythrocyte outer leaflet. DHE and Di4 form a FRET pair with a Förster distance that is approximately half the bilayer thickness, and therefore exchange energy much more efficiently when they are in the same leaflet (section 5.2 in SI). Thus, Di4-induced quenching of DHE fluorescence provides a readout of the relative outer leaflet enrichment of DHE, as a proxy for cholesterol's transbilayer distribution. Labeling conditions were tuned to ensure that overall sterol levels and membrane physical properties were unaffected (Figure S7) and that ~50% of DHE

is quenched in symmetric liposomes (Figure S8). Titration of Di4 into erythrocytes quenched DHE fluorescence, plateauing at ~64% reduction of DHE emission (Figure 3D). Quenching of the majority of DHE fluorescence by an externally applied quencher is consistent with the prediction that cholesterol is enriched in the exoplasmic leaflet of a living cell PM. This enrichment was eliminated by releasing lipid asymmetry with phorbol myristate acetate (PMA)[32] (Figure 3D), which scrambles PM phospholipids and cholesterol. Thus, computational predictions and experimental measurements suggest that cholesterol is enriched in the exoplasmic PM leaflet. We discuss caveats and other previous studies of cholesterol asymmetry in the caption of Figure S8.

Validation of the Cyto+ model

Our results suggest that the exoplasmic leaflet of mammalian PMs is relatively saturated, PL-depleted, and cholesterol-rich, a model of PM structure which we termed Cyto+. An atomistic simulation of this model was stable over >17 μsec with cholesterol continuing to partition away from the cytoplasmic leaflet, producing an exoplasmic leaflet with high density, lipid packing, and acyl chain order (Figure S9). To validate this emerging model of lipid organization and membrane structure, we developed methods to compare its structural and dynamical properties directly and quantitatively with those of living cell membranes. Previous measurements used the leaflet-specific fluorescence lifetime of Di4[2,33,34] to infer that the exoplasmic PM leaflet of mammalian cells is more tightly packed than the cytoplasmic. To examine how leaflet imbalances contribute to this observation, we calibrated experimental Di4 lifetimes to simulated lipid packing (i.e. area-per-lipid) using synthetic bilayers spanning a large range of lipid densities (Figure 4A). These two measures were highly correlated, allowing us to translate experimental Di4 lifetimes into a specific membrane structural parameter (area/lipid). We found that the exoplasmic PM leaflet of NIH 3T3 fibroblasts is ~20% more tightly packed (40.9 ± 2.31 Å^2/lipid) than the cytoplasmic leaflet (51.2 ± 2.22 Å^2/lipid) (Figure 4C–D, hatched bars). We directly compared these measurements to three distinct models of PM organization: in addition to the Cyto+ model (Figure 1E) derived from lipidomics and supported by DHE FRET measurements (Figure 3C–D), we simulated two alternative models with identical leaflet compositions but either equal (Equal) or greater (Exo+) PL abundance in the exoplasmic monolayer (Figure 4B, Table S5). For exoplasmic leaflets, lipid packing of the Cyto+ model matched nearly perfectly with the experimental measurement, while Exo+ was least accurate (Figure 4C, left). Further, the large difference in area/lipid between the two leaflets was successfully captured only by the Cyto+ model (Figures 4C, S10). We also simulated a scrambled version of Cyto+ (i.e. same lipid composition, but all lipids equally distributed between leaflets) and observed an intermediate lipid density between the exoplasmic and cytoplasmic leaflets, which matched very closely to experimental measurements of the fibroblast PM scrambled by ionomycin treatment (Figure 4D). Thus, leaflet structural differences in living cells are most consistent with an overabundance of PLs in the cytoplasmic leaflet (Cyto+).

Next, we investigated the correspondence in lipid *dynamics* between live cells and our emerging model of PM organization by comparing lipid diffusion in simulated membranes to measurements in cells (Figure 4E–H). Recently, it was reported that cholesterol diffuses much faster than PLs in both cultured cells and chordate embryos[6], which was notably different from synthetic, cell-derived, and computational model membranes, where the two lipids diffused similarly. Thus, fast cholesterol diffusion may be a hallmark of the lipid organization of living cell PMs[6]. We confirmed these findings in fibroblast PMs by measuring diffusion of fluorescently tagged sphingomyelin (TF-SM[35]) and cholesterol (TF-Chol[36,37]) via fluorescence correlation spectroscopy (FCS) (Figure 4E–F). TF-Chol diffused 1.6-fold faster than TF-SM and this difference was eliminated by scrambling PM lipids. Notably, similar trends were observable in the Cyto+ simulation: overall, cholesterol diffused 1.7-fold faster than SM and this difference was eliminated by lipid scrambling (Figure 4G). Further comparison between cholesterol and PL diffusion in each leaflet revealed that the observed trend is due to the much faster diffusion of cholesterol relative to PLs in the cytoplasmic PM leaflet (Figure 4H). In contrast, large differences between cholesterol and PL diffusion were not observed in any of the leaflets of the Exo+ and Equal models (Figure 4H). Consistently, cholesterol has been reported to diffuse faster than phospholipids only in simulations of highly unsaturated, loosely packed membranes with low cholesterol concentration[38]. Thus, the previously reported unexpected dynamic behavior of cholesterol in PMs appears to be consistent with the unusual lipid configurations proposed by the Cyto+ model.

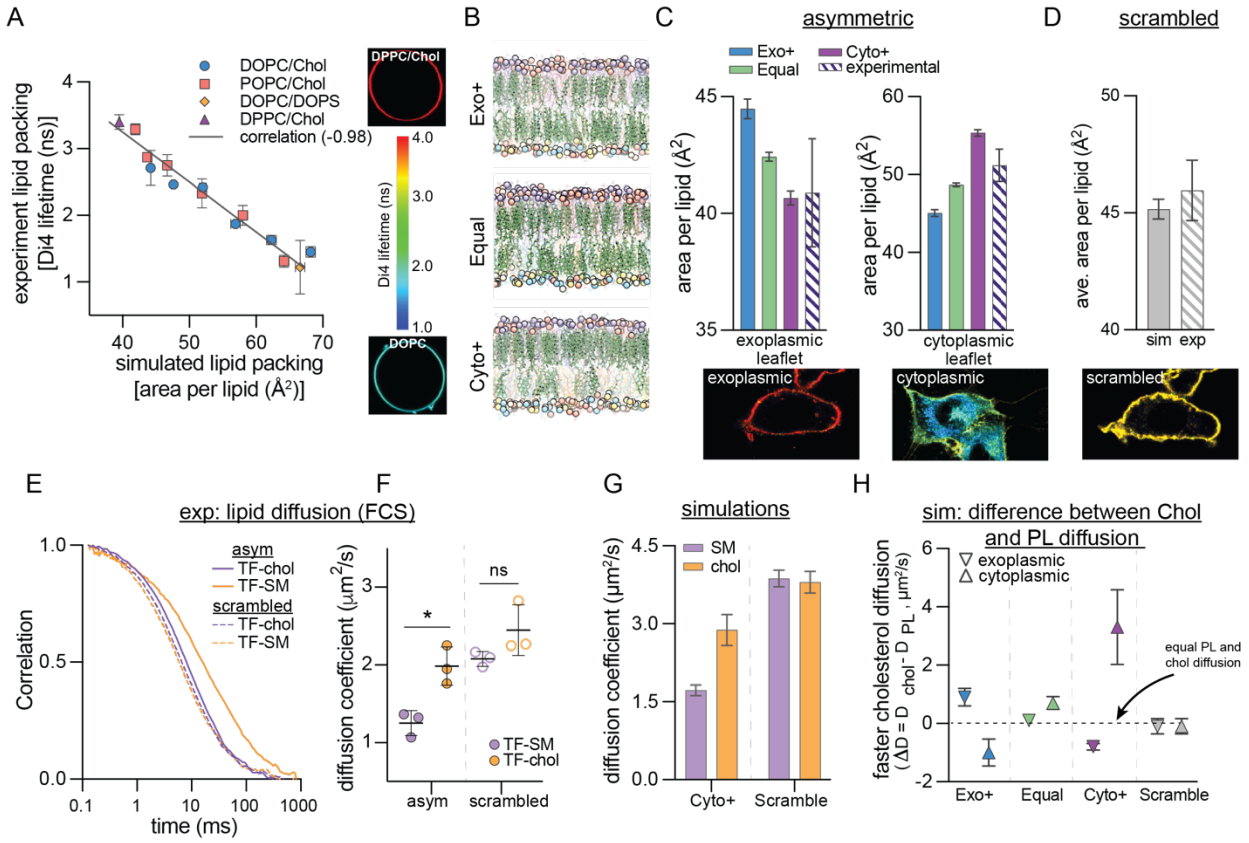

Figure 4 | Experimental validation of Cyto+ model. a, Calibration of Di4 lifetime, an experimental reporter of lipid packing measured in giant unilamellar vesicles (GUVs), with simulated area-per-lipid (APL) across a set of synthetic symmetric bilayers. Representative images of the least and most tightly packed GUVs are shown on the right. Color bar indicates Di4 lifetime. **b,** Snapshots of three simulated PM models having more PLs in their exoplasmic (top) or cytoplasmic (bottom) leaflets, or similar numbers of PLs in both leaflets (middle). Bilayer representation is the same as in Figure 1E. **c,** Leaflet packing densities (areas per lipid) from the three simulated PM models with different interleaflet PL abundances from **b** compared to experimental measurements in PMs of fibroblast cells. **d,** APL of the scrambled Cyto+ model compared to the experimentally scrambled (via ionophore treatment) fibroblast PM. **e,** Representative FCS curves for TF-SM and TF-chol in the PM of live NIH 3T3 cells before (asym) and after (scrambled) ionophore treatment. **f,** Corresponding diffusion coefficients of TF-SM and TF-chol calculated from FCS measurements. **g,** Diffusion coefficients of SM and cholesterol (chol) in the simulated Cyto+ membrane (left) and its scrambled counterpart (right). Cholesterol diffusion in Cyto+ represents the asymmetry-weighted average of the slowly diffusing population in the exoplasmic leaflet and the rapidly diffusing population in the cytoplasmic leaflet (Figure S13A). **h,** Difference between cholesterol and phospholipid diffusion (ΔD) in each leaflet of the simulated asymmetric PM models and the Cyto+ scrambled membrane.

Functional consequences of lipid imbalances

Having validated the compositional, structural, and dynamical features of the Cyto+ PM model against cell measurements, we examined the consequences of this unconventional lipid organization on membrane biophysical properties. The large lipid asymmetries suggest the presence of stress in the membrane and we first calculated the lateral pressure distribution in each leaflet (Figure 5A). While the bilayer has no net stress, the exoplasmic leaflet is compressed to 8.2 ± 0.8 mN/m while the cytoplasmic leaflet is under tension of the same magnitude. Such balanced compressive/tensile forces in an overall-tensionless membrane are termed 'differential stress'[39,40]. Here, differential stress arises both from differences in leaflet PL abundances and from cholesterol's preference for the outer leaflet. Lipid scrambling eliminates lipid asymmetries and alleviates the differential stress (Figure S11A).

Based on its significant lipid compression, we hypothesized that the cholesterol-enriched outer leaflet may constitute a robust barrier to transbilayer permeability. This hypothesis was tested first *in silico* by calculating the flux of water molecules through the bilayer (i.e. entering from one side and exiting from the

other). Comparing the Cyto+ model to its scrambled counterpart revealed that the scrambled PM was ~80% more permeable to water than the asymmetric PM (Figure 5B), highlighting a functional PM property arising from asymmetric lipid distribution, rather than overall lipid composition. To experimentally validate this observation, we investigated asymmetry-dependent PM permeability in erythrocytes. We measured transbilayer permeation of a small molecule, fluorescein diacetate (FDA), which becomes fluorescent only after encountering intracellular esterases[41]. Because transbilayer flux is the rate limiting step in this assay, the rate of fluorescence increase is directly proportional to membrane permeability[41]. Scrambled RBCs were 35% more permeable to FDA than asymmetric RBCs (Figure 5C), in agreement with the computational observation (Figure 5B). Simulations further suggested that this difference is likely due to the tightly packed outer leaflet, which presents the main barrier to transbilayer permeation in the Cyto+ model (Figure 5D). We observed many partial transitions of water molecules entering and exiting the cytosolic leaflet, but none from the exoplasmic leaflet (Figure 5D), illustrating the bipolar nature of the asymmetric membrane environment.

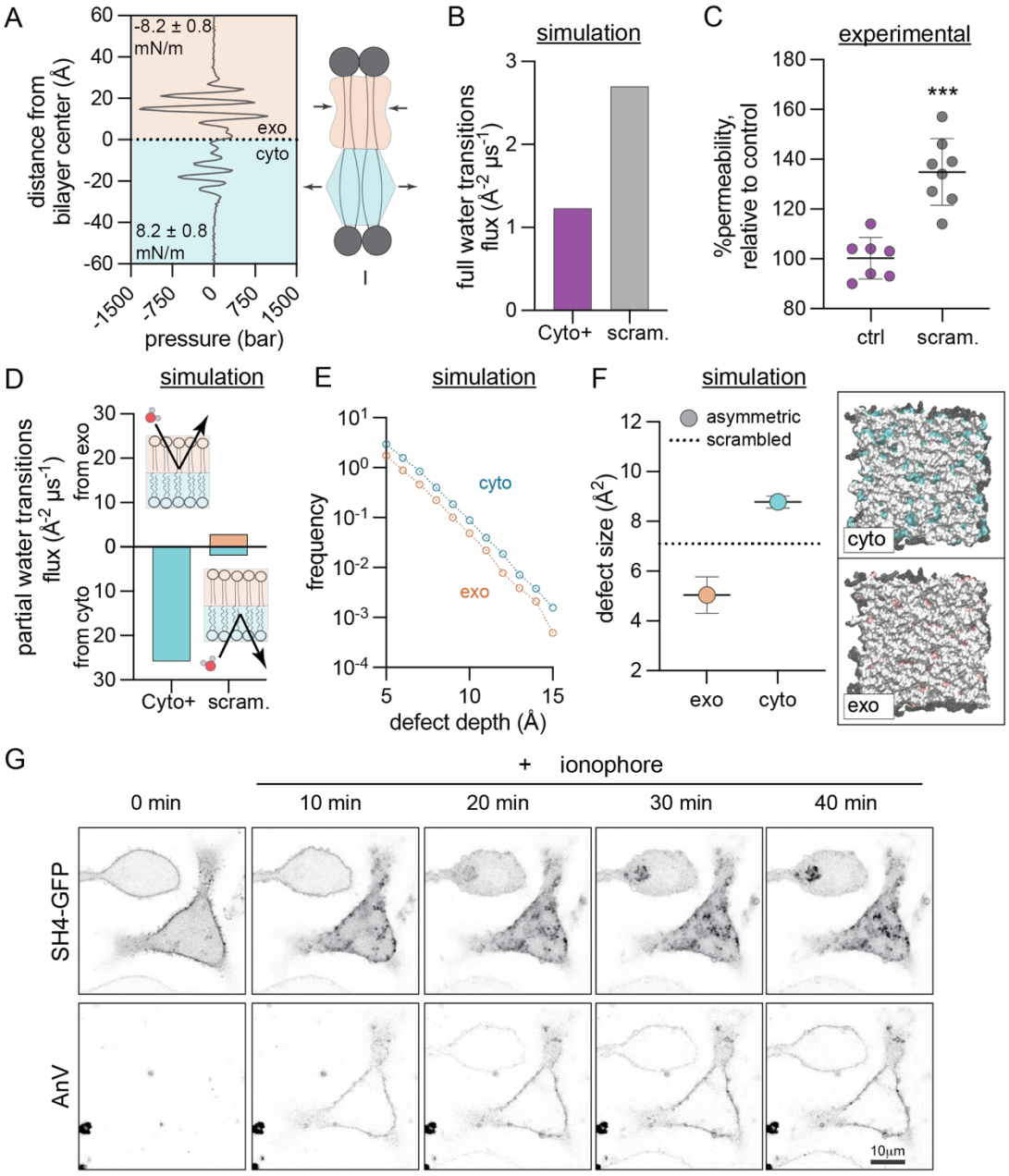

Figure 5 | Biophysical properties of the Cyto+ model. a, Transbilayer lateral pressure distribution in the simulated Cyto+ PM shows that the bilayer is differentially stressed, i.e. the exoplasmic leaflet (orange) is compressed while the cytoplasmic leaflet (cyan) is under tension of the same magnitude. **b,** Simulated water flux through Cyto+ compared to scrambled PM. **c,** Experimental permeability of erythrocyte

membranes to FDA. PMA-scrambled erythrocytes shown relative to untreated asymmetric controls. **d,** Flux of water molecules partially permeating the leaflets in simulations, i.e. entering the bilayer from the exoplasmic (top) or cytoplasmic (bottom) leaflet and exiting from the same leaflet. **e–f,** Hydrophobic defects in leaflets of simulated Cyto+ membrane and its scrambled counterpart. **e,** Histogram comparing defect sizes in the two Cyto+ leaflets. **f,** Defect size constants of deep defects in the Cyto+ leaflets compared to the scrambled bilayer (dashed line). Illustrative simulation snapshots of the Cyto+ bilayer viewed from the cyto or exo leaflet show shallow (in white) and deep (in color) solvent-exposed areas (defects) in surface representation. Opposite leaflet is shown in gray. **g,** Redistribution of lipidated peptide, the SH4 domain of Lyn (SH4-GFP), in RBL cells induced by PM scrambling with A23187, evidenced by concomitant exposure of PS monitored by the PS-marker AnxV-647.

The low lipid packing, high resting tension, and high permeability of the Cyto+ cytoplasmic leaflet suggest the likelihood of frequent hydrophobic defects, i.e. areas where the hydrophobic bilayer core is transiently exposed to water. Consistent with this prediction, simulations revealed that the Cyto+ cytoplasmic leaflet has more and larger deep hydrophobic defects than either the exoplasmic or scrambled leaflets (Figure 6E–F). Such defects have been previously implicated as "binding sites" for peripheral proteins that interact with membranes through hydrophobic moieties like lipid anchors[42] or amphipathic helices [43,44]. Our analysis predicts that the structure of the Cyto+ membrane facilitates peripheral protein binding to the cytoplasmic leaflet by promoting the insertion of hydrophobic anchors[42].

To test this hypothesis in live cells, we examined the asymmetry-dependent PM binding of a short lipidated peptide, the SH4 domain of the Src-family kinase Lyn, which associates with membranes via two lipid anchors (Figure 5G). To release PM asymmetry, cells were treated with A23187, a calcium ionophore that induces scrambling, evidenced by binding of the PS-marker Annexin V (AnxV) to the cell surface. In untreated cells, AnxV did not bind, and the peptide was localized to the PM. Ionophore treatment produced the predicted AnxV binding, but also a concomitant detachment of the peptide from the PM and relocation to the cytosol and intracellular organelles (Figure 5G). The same behavior was observed for two other peptides representative of the membrane anchoring domain of H-Ras (Figure S12). This general desorption of lipidated peptides from the PM after scrambling suggests that their PM association is mediated by the deep hydrophobic defects that arise in the tensed, cholesterol-poor cytosolic leaflet.

Discussion and broader implications

We report a previously unrecognized feature of mammalian PMs: major differences in total phospholipid abundance between bilayer leaflets, facilitated by asymmetric cholesterol distribution. High cholesterol concentrations enable bilayer tolerances for the large PL imbalances revealed by our lipidomics measurements (Figures 1-2), while cholesterol extraction compromises membrane integrity (Figure 2C–E). While the relative paucity of PLs in exoplasmic leaflets was unexpected and had not been previously reported, re-analysis of previous data on lipid asymmetry reveals confirms our observations (Table S1, Figure 1D). This result was perceived as physically unrealistic due to the usually implicit assumption that leaflets with equal areas must also contain similar PL abundances [19]. This assumption is fundamental to current conceptions of biomembrane lipid distributions, underlying the interpretations and design of nearly all experiments and models. Theory[29], simulations, and our observations reveal that this assumption is generally invalid and likely inaccurate for mammalian PMs.

Cholesterol sustains interleaflet PL imbalances by accumulating in the PL-poor leaflet. This capability is enabled by cholesterol's uniquely rapid flipping between leaflets. Cholesterol's equilibrium distribution is determined by a balance of its tendency to "fill gaps" in the underpopulated leaflet, its preference for saturated lipids, and entropic effects favoring symmetric arrangement (Figure 3A–B), as described in a recent elegant theory[45,46]. As exoplasmic leaflets of cell PMs are not only more saturated but also relatively PL-poor, cholesterol is predicted to enrich in the exoplasmic leaflet. Consistent with this reasoning and theoretical predictions[29], we observe enrichment of cholesterol in the erythrocyte outer leaflet (Figure 3D). This result is consistent with a recent study that used engineered sensors to measure much higher cholesterol concentrations in the outer PM leaflet[47], a conclusion that was questioned on the theoretical grounds that rapid cholesterol flip-flop would appear to preclude significant cholesterol disparity between leaflets[4]. Our findings reveal a simple mechanism that not only allows, but demands, interleaflet cholesterol imbalances. While other studies have reported on cholesterol's distribution in cell PMs (Figure S8 caption), our model provides a mechanistic explanation for cholesterol's ultimate transbilayer distribution.

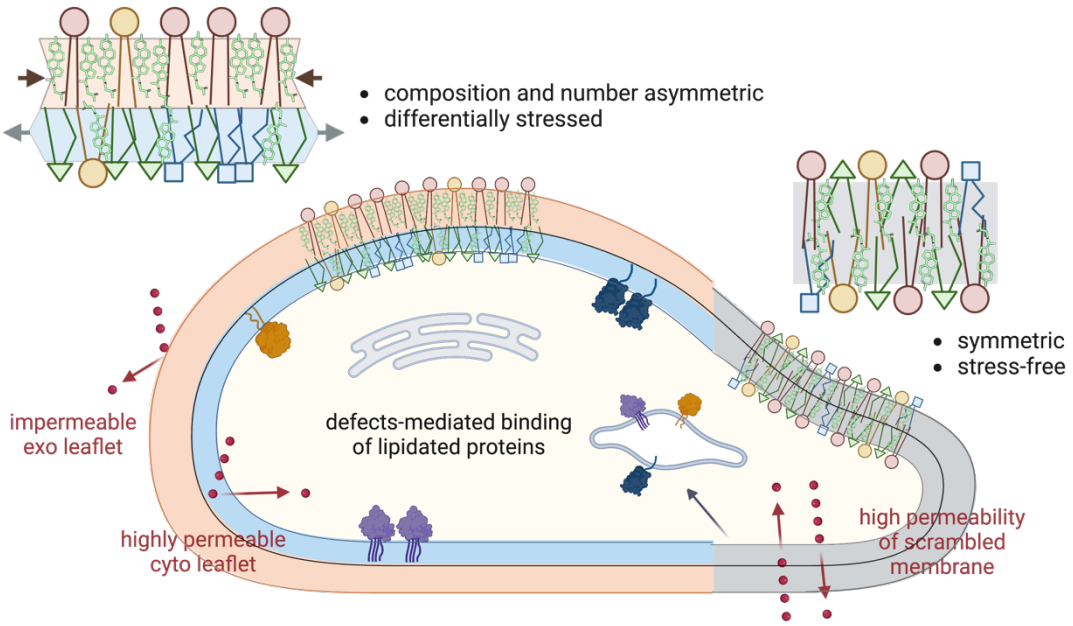

Figure 6 | Emerging model of lipid and cholesterol organization in mammalian plasma membranes. The plasma membrane bilayer is asymmetric both in composition and total abundance of phospholipids and cholesterol, with fewer phospholipids and more cholesterol in the exoplasmic leaflet. This organization produces differential stress, with a compressed outer leaflet and the inner leaflet under tension. Consequences of this arrangement include: (1) differential permeablity of the two leaflets with relative impermeability of the asymmetric membrane; and (2) preferential interaction of lipidated proteins with the tensed cytoplasmic leaflet and subsequent detachment from the PM upon lipid scrambling.

Experimental measurements of leaflet lipid packing support our model of a PM with a PL-rich and cholesterol-poor cytoplasmic leaflet (Figures 4A–D, S10). Similarly, experimentally observed fast cholesterol diffusion (Figure 4E–F) appears to be a signature of a differentially stressed, unsaturated lipid-rich, cholesterol-poor leaflet (Figures 4G–H, S13), consistent only with the Cyto+ model. The inference that the cytoplasmic PM leaflet is under tension may seem contradictory with its relative over-abundance of PLs (Figure 1). However, in the presence of cholesterol, such stresses are not solely the result of lipid imbalances, but rather several complex drivers of cholesterol distribution (Figure 3), which can induce, rather than alleviate, leaflet tension (Figure S6). It may be surprising that a membrane with one compressed and one tensed leaflet would not spontaneously deform (i.e. bend) to alleviate these stresses. However, differential stress can be balanced by curvature stresses arising from differences in the preferred (spontaneous) curvatures of leaflet lipids[5], as is the case for the Cyto+ PM model (Figure S11B). Further, other mechanical constrains (most prominently the cytoskeleton) may prevent spontaneous bending in living cells.

The asymmetric distributions of PLs and cholesterol in the two PM leaflets revealed by our analyses have far-reaching implications for biomembrane structure and function (Figure 6). The physicochemical asymmetry of the two PM leaflets provides cells with novel regulatory modes, namely the possibility of tuning leaflet packing, tension, and dynamics independent of lipid headgroup chemistry. These lipid arrangements may underlie PM properties such as low permeability and regulated binding of lipidated proteins (Figure 6). We therefore posit that abundance asymmetry of membrane components presents a previously unexplored dimension of PM organization and function.

Main Text References:

1 Kusumi, A. *et al.* Dynamic organizing principles of the plasma membrane that regulate signal transduction: commemorating the fortieth anniversary of Singer and Nicolson's fluid-mosaic model. *Annu. Rev. Cell Dev.Biol.* **28**, 215-250 (2012).

2 Lorent, J. H. *et al.* Plasma membranes are asymmetric in lipid unsaturation, packing and protein shape. *Nat Chem Biol* **16**, 644-652 (2020). https://doi.org:10.1038/s41589-020-0529-6

3 Verkleij, A. J. *et al.* The asymmetric distribution of phospholipids in the human red cell membrane. A combined study using phospholipases and freeze-etch electron microscopy. *Biochim Biophys Acta* **323**, 178-193 (1973).

4 Steck, T. L. & Lange, Y. Transverse distribution of plasma membrane bilayer cholesterol: Picking sides. *Traffic* **19**, 750-760 (2018). https://doi.org:10.1111/tra.12586

5 Hossein, A. & Deserno, M. Spontaneous Curvature, Differential Stress, and Bending Modulus of Asymmetric Lipid Membranes. *Biophys. J.* **118**, 624-642 (2020). https://doi.org:10.1016/j.bpj.2019.11.3398

6 Pinkwart, K. *et al.* Nanoscale dynamics of cholesterol in the cell membrane. *The Journal of biological chemistry* **294**, 12599-12609 (2019). https://doi.org:10.1074/jbc.RA119.009683

7 Singer, S. J. & Nicolson, G. L. The fluid mosaic model of the structure of cell membranes. *Science* **175**, 720-731 (1972).

8 Devaux, P. F. Static and dynamic lipid asymmetry in cell membranes. *Biochem. J.* **30**, 1163-1173 (1991).

9 Bretscher, M. S. Asymmetrical lipid bilayer structure for biological membranes. *Nat New Biol* **236**, 11-12 (1972).

10 Nagata, S., Sakuragi, T. & Segawa, K. Flippase and scramblase for phosphatidylserine exposure. *Curr Opin Immunol* **62**, 31-38 (2020). https://doi.org:10.1016/j.coi.2019.11.009

11 Sakuragi, T. & Nagata, S. Regulation of phospholipid distribution in the lipid bilayer by flippases and scramblases. *Nat. Rev. Mol. Cell Biol.*, 1-21 (2023). https://doi.org:10.1038/s41580-023-00604-z

12 van den Eijnde, S. M. *et al.* Transient expression of phosphatidylserine at cell-cell contact areas is required for myotube formation. *J Cell Sci* **114**, 3631-3642 (2001).

13 Mercer, J. & Helenius, A. Vaccinia virus uses macropinocytosis and apoptotic mimicry to enter host cells. *Science* **320**, 531-535 (2008). https://doi.org:10.1126/science.1155164

14 Elliott, J. I. *et al.* Membrane phosphatidylserine distribution as a non-apoptotic signalling mechanism in lymphocytes. *Nat. Cell Biol* **7**, 808-816 (2005). https://doi.org:10.1038/ncb1279

15 Doktorova, M., Symons, J. L. & Levental, I. Structural and functional consequences of reversible lipid asymmetry in living membranes. *Nat. Chem. Biol* **16**, 1321-1330 (2020). https://doi.org:10.1038/s41589-020-00688-0

16 Bevers, E. M. & Williamson, P. L. Getting to the Outer Leaflet: Physiology of Phosphatidylserine Exposure at the Plasma Membrane. *Physiol Rev* **96**, 605-645 (2016). https://doi.org:10.1152/physrev.00020.2015

17 Zwaal, R. F., Roelofsen, B., Comfurius, P. & van Deenen, L. L. Organization of phospholipids in human red cell membranes as detected by the action of various purified phospholipases. *Biochim. Biophys. Acta* **406**, 83-96 (1975). https://doi.org:10.1016/0005-2736(75)90044-9

18 Renooij, W., Van Golde, L. M., Zwaal, R. F., Roelofsen, B. & Van Deenen, L. L. Preferential incorporation of fatty acids at the inside of human erythrocyte membranes. *Biochim. Biophys. Acta* **363**, 287-292 (1974). https://doi.org:10.1016/0005-2736(74)90069-8

19 Rawyler, A., van der Schaft, P. H., Roelofsen, B. & Op den Kamp, J. A. Phospholipid localization in the plasma membrane of Friend erythroleukemic cells and mouse erythrocytes. *Biochem. J.* **24**, 1777-1783 (1985). https://doi.org:10.1021/bi00328a031

20 Van der Schaft, P. H., Roelofsen, B., Op den Kamp, J. A. & Van Deenen, L. L. Phospholipid asymmetry during erythropoiesis. A study on Friend erythroleukemic cells and mouse reticulocytes. *Biochim. Biophys. Acta* **900**, 103-115 (1987). https://doi.org:10.1016/0005-2736(87)90282-3

21 Lange, Y., Dolde, J. & Steck, T. L. The rate of transmembrane movement of cholesterol in the human erythrocyte. *The Journal of biological chemistry* **256**, 5321-5323 (1981).
22 Bruckner, R. J., Mansy, S. S., Ricardo, A., Mahadevan, L. & Szostak, J. W. Flip-flop-induced relaxation of bending energy: implications for membrane remodeling. *Biophys J* **97**, 3113-3122 (2009). https://doi.org:10.1016/j.bpj.2009.09.025
23 Huang, Z. & London, E. Effect of cyclodextrin and membrane lipid structure upon cyclodextrin-lipid interaction. *Langmuir* **29**, 14631-14638 (2013). https://doi.org:10.1021/la4031427
24 Zidovetzki, R. & Levitan, I. Use of cyclodextrins to manipulate plasma membrane cholesterol content: evidence, misconceptions and control strategies. *Biochim. Biophys. Acta* **1768**, 1311-1324 (2007). https://doi.org:10.1016/j.bbamem.2007.03.026
25 McGraw, C., Yang, L., Levental, I., Lyman, E. & Robinson, A. S. Membrane cholesterol depletion reduces downstream signaling activity of the adenosine A2A receptor. *Biochim Biophys Acta Biomembr* **1861**, 760-767 (2019). https://doi.org:10.1016/j.bbamem.2019.01.001
26 Arashiki, N. *et al.* An Unrecognized Function of Cholesterol: Regulating the Mechanism Controlling Membrane Phospholipid Asymmetry. *Biochem. J.* **55**, 3504-3513 (2016). https://doi.org:10.1021/acs.biochem.6b00407
27 Miettinen, M. S. & Lipowsky, R. Bilayer Membranes with Frequent Flip-Flops Have Tensionless Leaflets. *Nano Lett* **19**, 5011-5016 (2019). https://doi.org:10.1021/acs.nanolett.9b01239
28 Almeida, P. F. Thermodynamics of lipid interactions in complex bilayers. *Biochim. Biophys. Acta* **1788**, 72-85 (2009). https://doi.org:10.1016/j.bbamem.2008.08.007
29 Varma, M. & Deserno, M. Distribution of cholesterol in asymmetric membranes driven by composition and differential stress. *Biophys. J.* **121**, 4001-4018 (2022). https://doi.org:10.1016/j.bpj.2022.07.032
30 McIntosh, A. L. *et al.* Fluorescence techniques using dehydroergosterol to study cholesterol trafficking. *Lipids* **43**, 1185-1208 (2008). https://doi.org:10.1007/s11745-008-3194-1
31 Pourmousa, M. *et al.* Dehydroergosterol as an analogue for cholesterol: why it mimics cholesterol so well-or does it? *J. Phys. Chem. B* **118**, 7345-7357 (2014). https://doi.org:10.1021/jp406883k
32 Wesseling, M. C. *et al.* Novel Insights in the Regulation of Phosphatidylserine Exposure in Human Red Blood Cells. *Cell Physiol Biochem* **39**, 1941-1954 (2016). https://doi.org:10.1159/000447891
33 Jin, L. *et al.* Characterization and application of a new optical probe for membrane lipid domains. *Biophys. J.* **90**, 2563-2575 (2006). https://doi.org:10.1529/biophysj.105.072884
34 Owen, D. M. *et al.* Fluorescence lifetime imaging provides enhanced contrast when imaging the phase-sensitive dye di-4-ANEPPDHQ in model membranes and live cells. *Biophys. J.* **90**, L80-82 (2006). https://doi.org:10.1529/biophysj.106.084673
35 Sezgin, E. *et al.* Partitioning, diffusion, and ligand binding of raft lipid analogs in model and cellular plasma membranes. *Biochim. Biophys. Acta* **1818**, 1777-1784 (2012). https://doi.org:10.1016/j.bbamem.2012.03.007
36 Holtta-Vuori, M. *et al.* BODIPY-cholesterol: a new tool to visualize sterol trafficking in living cells and organisms. *Traffic* **9**, 1839-1849 (2008). https://doi.org:10.1111/j.1600-0854.2008.00801.x
37 Wustner, D., Lund, F. W., Rohrl, C. & Stangl, H. Potential of BODIPY-cholesterol for analysis of cholesterol transport and diffusion in living cells. *Chem. Phys. Lipids* **194**, 12-28 (2016). https://doi.org:10.1016/j.chemphyslip.2015.08.007
38 Javanainen, M. & Martinez-Seara, H. Rapid diffusion of cholesterol along polyunsaturated membranes via deep dives. *Phys. Chem. Chem. Phys.* **21**, 11660-11669 (2019). https://doi.org:10.1039/c9cp02022e
39 Varma, M. & Deserno, M. Distribution of cholesterol in asymmetric membranes driven by composition and differential stress. *Biophys J* (2022). https://doi.org:10.1016/j.bpj.2022.07.032
40 Doktorova, M. & Levental, I. Cholesterol's balancing act: Defying the status quo. *Biophys J* (2022). https://doi.org:10.1016/j.bpj.2022.08.036
41 Levental, K. R. *et al.* Lipidomic and biophysical homeostasis of mammalian membranes counteracts dietary lipid perturbations to maintain cellular fitness. *Nat. Commun* **11**, 1339 (2020). https://doi.org:10.1038/s41467-020-15203-1

42 Larsen, J. B. *et al.* Membrane curvature enables N-Ras lipid anchor sorting to liquid-ordered membrane phases. *Nat Chem Biol* (2015). https://doi.org:10.1038/nchembio.1733
43 Cui, H., Lyman, E. & Voth, G. A. Mechanism of membrane curvature sensing by amphipathic helix containing proteins. *Biophys. J.* **100**, 1271-1279 (2011). https://doi.org:10.1016/j.bpj.2011.01.036
44 Vanni, S. *et al.* Amphipathic lipid packing sensor motifs: probing bilayer defects with hydrophobic residues. *Biophys. J.* **104**, 575-584 (2013). https://doi.org:10.1016/j.bpj.2012.11.3837
45 Foley, S. L., Varma, M., Hossein, A. & Deserno, M. Elastic and thermodynamic consequences of lipid membrane asymmetry. *Emerg Top Life Sci* **7**, 95-110 (2023). https://doi.org:10.1042/ETLS20220084
46 Varma, M. & Deserno, M. Distribution of cholesterol in asymmetric membranes driven by composition and differential stress. *Biophys J* **121**, 4001-4018 (2022). https://doi.org:10.1016/j.bpj.2022.07.032
47 Liu, S. L. *et al.* Orthogonal lipid sensors identify transbilayer asymmetry of plasma membrane cholesterol. *Nat. Chem. Biol* **13**, 268-274 (2017). https://doi.org:10.1038/nchembio.2268

Methods

Lipidomics

Human erythrocytes (freshly isolated and intact) were treated with two enzymes, phospholipase A2 (PLA2, Sigma) and sphingomyelinase (SMase, Sigma) to digest exclusively the lipid species on the exoplasmic PM leaflet as detailed in [1] and summarized in SI. Enzyme-treated cells were analyzed with shotgun electron spray ionization with tandem MS-MS (ESI-MS/MS) by Lipotype and compared to untreated controls to determine the abundance of ~400 unique phospholipid species, including glycosphingolipids, on the exoplasmic leaflet via the extent of digestion. MS data acquisition and analysis were performed as in [1] and summarized in Supplemental Information.

Phospholipid extraction from synthetic liposomes

Large unilamellar vesicles (LUVs) composed of POPC (Avanti) with 0, 20 and 40% Chol (Avanti) were prepared at a concentration of 24 mM as described in [2]. Hydroxypropyl-alpha-cyclodextrin (HPαCD, Sigma Aldrich) was dissolved in water at a nominal concentration of 500 mM and spun through a pre-washed centricon filter device (Ultra-15, 100,000 Da molecular weight cutoff; Amicon; MilliporeSigma) to remove any aggregates as detailed in SI. POPC extraction from the liposomes was achieved by mixing 170 μM LUVs with increasing amounts of HPαCD at room temperature. Light scattering was measured on an Anton Paar Litesizer 100 at 22°C. Subsequently, each sample was spun through the same Centricon filter device as above; the filtrate was transferred to a glass culture tube and spiked with 2 μl of DMPC (Avanti, 25.27 mg/mL in chloroform); the sample was frozen overnight and lyophilized the next day. The lyophilized powder was subjected to acid-catalyzed methanolysis to extract the fatty acid methyl esters (FAMEs) and their analysis was done on an Agilent 5890A gas chromatograph (Santa Clara, CA) with a 5975C mass-sensitive detector operating in electron-impact mode and an HP-5MS capillary column (30 m x 0.25 mm, 0.25-mm film thickness) as described in [2] and summarized in SI. The respective peak areas of the FAMEs corresponding to the myristoyl chain of DMPC and the palmitoyl chain of POPC were recorded and used to calculate the normalized amount of POPC in the sample.

Cell culture

RBL-2H3 cells were purchased from ATCC and grown in Eagle's Minimum Essential Medium (EMEM) media (Gibco) with 10% fetal bovine serum (FBS, Genessee) and 1% penicillin-streptomycin (Gibco). 3T3 cells were grown in Dulbecco's Modified Eagle Medium (DMEM) supplemented with 10% FBS.

Cholesterol extraction from cells

RBL-2H3 cells were washed twice with CaR buffer (145 mM NaCl, 5 mM KCl, 10 mM HEPES at pH 7.4), then incubated with CaR buffer containing either 2 mM $CaCl_2$ or 2 mM EDTA in the absence or presence of 6 mM MβCD (Thermo Fisher). For monitoring PS exposure and dextran permeability, the buffer also

contained LactC2-mClover and Rhodamine-dextran (Sigma-Aldrich) as detailed in SI. For PI permeability measurements, the buffer contained propidium iodide (Alfa Aesar). Cells and buffer were incubated at room temperature (20–22°C) and imaged at the indicated time points (30, 60, and 90 minutes). Confocal fluorescence imaging of cells was performed at 21°C using a Nikon C2+ point scanning system attached to a Nikon Eclipse Ti2-E microscope equipped with a Plan Apo Lambda 60X oil immersion objective and a Bioptech objective cooling collar. Imaging data was analyzed with FIJI as described in SI.

DHE distribution in erythrocytes

Human erythrocytes were isolated from healthy donors with informed consent and suspended in Ringer's solution (125 nM NaCl; 5 mM KCl; 3 mM CaCl2; 1 mM MgSO4; 30 mM HEPES; 5 mM glucose; pH 7.4). DHE (Sigma Aldrich) was dissolved in MβCD (160 mM in Ringer's solution) at 1:8 ratio at room temperature and centrifuged briefly to remove any aggregates. 3.5×10^8 cells/mL were suspended in a mixture of the DHE/MβCD solution and free MβCD in Ringer's solution for final concentrations of 50 μM DHE and 1.2 mM MβCD, unless otherwise specified, and nutated for 10 minutes at room temperature. The sample was washed 3 times with Ringer's solution with 2,000 rcf spins for 3 minutes at room temperature. Di4 (Di-4-ANEPPDHQ, Thermo Fisher, dissolved in ethanol) was diluted 10-fold in Ringer's solution to 100 µg/mL and added to cells (1.5×107 cells/mL) at room temperature. Di4 addition was directly followed by measurement of DHE emission spectrum on a PTI fluorimeter at 37 °C. To minimize inner filter effect (IFE), measurements were taken using a 10 × 2 mm pathlength cuvette oriented with 2 mm pathlength facing detector and minimal sample volume. Excitation and emission slits were open to 5 nm, the gain was optimized for increased signal, and measurements were taken at a scan rate of 0.1 s/nm to minimize photobleaching. DHE quenching was monitored by measuring the decrease in emission at 385 nm upon addition of Di4 until a plateau was reached. The relative amount of quenched DHE fluorescence at this plateau was used to quantify the fraction of DHE (and therefore, cholesterol) residing in the outer leaflet of the membrane.

Quantification of sterol content in erythrocytes

To quantify total sterol content in the erythrocyte membrane, lipids were first extracted using a two-step extraction protocol [3]. Amplex Red cholesterol assay was performed (according to manufacturer instructions; Invitrogen) to determine the abundance of cholesterol and DHE. Each reading was normalized to cell count. Technical triplicates were measured for each sample. All values are normalized to untreated cells and are the average and standard deviations from at least two independent biological replicates.

DHE distribution in synthetic liposomes

Symmetric large unilamellar vesicles (LUVs) at 25 mg/mL lipid were prepared as in [2]. Unsaturated lipids were extruded at room temperature, and multicomponent mixtures were extruded at 45°C. For DHE-containing vesicles, DHE was incorporated into the lipid mixture in organic solvent (prior to drying and hydration). DHE titrations were performed by replacing cholesterol for DHE and keeping total sterol concentration constant. Measurements were done on a PTI fluorimeter as described above. 1 μL of 2.5 mg/mL LUVs was diluted into 165 μL of Ringer's solution, yielding ~15 µg/mL LUVs in the cuvette. If Di4 was not already incorporated into the liposomes, Di4 (stock dissolved in ethanol) was first diluted 10x in Ringer's solution, then 1.5 µL from the diluted solution were added to the LUV suspension and pipette mixed. Samples were checked for risk of photobleaching via time-based emission scans. DHE emission spectra was obtained by excitation at 310 nm and emission between 340–500 nm at 37 °C. Measurements with externally added Di4 were taken immediately after addition with each sample of LUVs discarded after each measurement and the cuvette thoroughly washed.

DHE self-quenching in liposomes

Vesicles were prepared following the rapid solvent exchange (RSE) protocol as described previously [4] and summarized in the SI. The fluorescence intensity was measured on a Horiba Fluorolog 3 spectrofluorometer by exciting the sample at 327.8 nm and collecting the emission in the range 340–640 nm. The excitation and emission slits were set to 2.5 and 3 nm, respectively and the integration time was 0.1 s. The 2 mL sample was continuously stirred during the measurement via a flea stir bar placed in the cuvette.

To compare the DHE fluorescence across samples, the full spectrum of each sample was first normalized by subtracting the spectrum of the respective lipid-only (without DHE) sample. The normalized spectra

were then integrated to obtain total DHE fluorescence, and the value was corrected for the volume difference measured during sample preparation. Integration of the DHE spectra, as opposed to using the fluorescence at a fixed wavelength, was necessary due to changes in the shape of the spectrum as a result of the formation of various DHE configurational states at higher DHE concentrations [5] (Figure S15).

Scrambling of erythrocyte membranes

To scramble erythrocyte membranes, equal number of cells (~3.4×10^8 cells/mL) were incubated with 100 μM phorbol-12-myristate acetate (PMA, Cayman Chemicals) in Ringer's solution for 10 minutes on nutate at room temperature. Any additions and measurements were performed immediately afterwards.

Permeability measurements in erythrocytes

2×10^6 cells/mL were resuspended in Ringer's solution, 1 µg/mL fluorescein diacetate (Cayman Chemicals, 1 mg/mL in acetone) was added and mixed by pipetting, and the fluorescence intensity was read at 450 nm excitation and 510 nm emission over a period of 1 min (at 1 Hz) with 5 nm excitation and emission slits. In each sample, fluorescence increased linearly, thus the slope of fluorescence over time remained constant over the 60 s, consistent with a constant flux (Q) (Figure S16). The permeability coefficient (P) is defined by Fick's Law as $Q = PA(\mathrm{C_{out}} - \mathrm{C_{in}})$ where P is permeability, A is the area of the membrane, and $\mathrm{C_{out}}$ and $\mathrm{C_{in}}$ are the concentrations of the solute outside and inside the cells, respectively. In our experiments, $\mathrm{C_{in}} = 0$ because FDA is quickly converted into fluorescein upon entering the cell. With equal A (due to same number of cells and cellular membranes) and $\mathrm{C_{out}}$ across samples, permeability can be directly compared between conditions by normalizing to control samples.

Peptide binding to cell plasma membranes

RBL cells at 70-80% confluency were harvested with Trypsin (Gibco) and transfected with the respective plasmids via electroporation (see SI for details). After 24 hours, cells were washed with PBS buffer, then maintained in Annexin V buffer (150 mM NaCl, 10 mM HEPES, 2 mM CaCl2, pH 7.4, with 100x diluted Annexin V AF647 from ThermoFisher, #A23204). Ionophore A23187 (Cayman, #11016) diluted in Annexin V buffer was added to the cells with a final concentration of 6 µM. Cells were imaged immediately after the addition of A23187 with a 63X water immersion objective on a Leica SP8 confocal microscope. Images were taken with 10 second intervals for up to 40 minutes.

Measurement of cholesterol and lipid diffusion in nucleated cells

3T3 cells were seeded on glass-bottom dishes two days before the diffusion experiments. For fluorescent labeling, the fluorescent lipid analogs (Topfluor SM and Topfluor Chol, Avanti Polar Lipids) were first dissolved in DMSO at a final concentration of 1 mg/ml. Before labelling, the cells were washed twice with L-15 medium to remove the full media. Later the fluorescent analogs were mixed with L-15 medium at a 1:1000 ratio (final concentration of 1 µg/ml). The cells were incubated with this suspension for three to five minutes at room temperature, then washed with L-15 twice followed by fluorescence correlation spectroscopy (FCS) measurements. To measure diffusion of scrambled plasma membranes, 3T3 cells were treated with 3 µM A23187 ionophore for eight to ten minutes at 37°C before lipid labelling. Scrambling was confirmed by AnnexinV-AF647 labelling (ThermoFisher A23204). FCS was carried out using a Zeiss LSM 780 microscope with a 40X water immersion objective (numerical aperture 1.2) as described previously [6].

Measurement of Di4 lifetime in GUVs and cells

Giant unilamellar vesicles (GUVs) were prepared by electroformation, and Di4 was added to them externally as described previously [1]. The samples were imaged at room temperature on a Leica SP8 FLIM confocal microscope with excitation at 485 nm with an 80 MHz pulsed laser, and the lifetime collected in an emission window of 550–800nm. The data was fit using a 2-component reconvolution fit, and the intensity-weighted average lifetime was reported.

To measure Di4 lifetime in the outer leaflet of 3T3 cells, cells were incubated with 1 µg/mL Di4 at 4 °C for 8 min in CaR buffer (145 mM NaCl, 5 mM KCl, 10 mM HEPES) supplemented with 2 mM $CaCl_2$ and 2 mM $MgCl_2$ at pH 8.0. Cells were briefly washed twice in the same buffer at ambient temperature before imaging at room temperature. To prevent contaminating signal from internalization of the dye, all images were acquired within 20 minutes. To measure Di4 lifetime in scrambled plasma membranes, 3 mM A23187

was added to cells in the same CaR buffer for 15 minutes at 37 °C. Following this treatment, the cells were washed with CaR buffer, with Di4 incubation and imaging as above.

Molecular Dynamics simulations

All bilayer simulations were initially constructed and equilibrated with CHARMM-GUI [7]. Coarse-grained (CG) simulations were carried out in Gromacs [8] with the Martini 2.2 force-field [9] and all-atom simulations were run with NAMD [10] and the CHARMM36 force-field [11] unless otherwise noted. All simulation parameters and solvation details are described in the SI.

Tolerance for PL imbalance, CG simulations. A series of asymmetric membranes were constructed with a lipid composition mimicking that of the erythrocyte plasma membrane but with fixed PL imbalance (35% more PLs in the cytoplasmic leaflet) and varying amounts of Chol (ranging between 10 and 50 mol% of all membrane lipids). Table S2 summarizes the initial lipid make-up of the membranes.

After equilibration all cholesterol molecules were replaced with a recently optimized cholesterol model [12] which circumvents previously reported problems with cholesterol in Martini [13], and simulated for 10 μs. Cholesterol interleaflet distribution was determined from the tilt of the Chol molecules. Phospholipids did not change their leaflet residence during the simulations. The maximal phosphate-to-phosphate distance was calculated from the difference between the minimum and maximum z positions of all phosphate (PO4) beads in each frame of the trajectory.

Effects of PS flip-flop on tension, AA simulations. To evaluate the effect of flipping PS lipids to the opposite leaflet, we performed a series of AA simulations in which the total number of lipids in the bilayer remained fixed and we mimicked PS flipping by generating different starting configurations with respect to PS interleaflet distribution. The effects of Chol flipping were examined in the same way. The lipid compositions, system sizes and total trajectory lengths of the simulations are listed in Table S3. The tension in each leaflet was calculated as described previously [14] and summarized in the SI. Errors on the tension were estimated with a bootstrapping approach in which a dataset with the same total number of frames was reconstructed by picking frames from the original dataset at random and allowing repetitions. The pressure profile and leaflet tensions were then obtained from the resampled data. This procedure was repeated multiple times to obtain the error (i.e. standard deviation) of the leaflet tension.

Cholesterol distribution in simpler asymmetric membranes. To examine the effects of phospholipid imbalance and tension on cholesterol distribution in asymmetric membranes, we performed a series of simulations first CG and then in AA representations.

Initially, 8 asymmetric bilayers with one saturated leaflet (composed of 100 DPPC lipids) and one unsaturated leaflet (composed of a varying number of DAPC lipids), each containing 30 mol% cholesterol (Chol), were constructed and simulated (Table S4). To count the number of lipids and Chol in each leaflet, the bilayer was first centered so that the bilayer midplane was in the center of the simulation box in every frame. Then, the DAPC and DPPC lipids whose phosphate (PO4) beads were below/above the bilayer center were counted as belonging to the bottom/top leaflets respectively. Chol was treated the same way except that its headgroup OH bead was used instead. Chol distribution equilibrated within the first few μs in all systems and all reported quantities are averaged over the last 5 μs of the trajectories.

The equilibrated lipid distributions from the CG simulations were used to construct and simulate corresponding all-atom bilayers (Table S4) for detailed analysis of leaflet tension.

PM models: AA simulations. To examine the effects of PL imbalance on cholesterol interleaflet distribution and bilayer properties we built 3 asymmetric models of the plasma membrane. Each had ~40 mol% overall cholesterol and the same leaflet phospholipid compositions modeled after the lipidomics results, but differed in the relative total abundances of PLs in their two leaflets (see Table S5 for the exact numbers and types of lipids in each leaflet). The bilayers were constructed and simulated as described in the SI.

Prior to analysis each system was centered so that the bilayer was in the middle of the simulation box and the average (x,y,z) of the bilayer midplane was at (0,0,0). The last 1.2 μs of the simulations (with output

frequency of 120 ps) were used for all analysis except for lipid diffusion which was calculated over the trajectory lengths indicated in Table S6 with output frequency of 20 ps.

To analyze the permeability of a membrane we first identified all water molecules that at some point in time were found 10 Å or more below the instantaneous average z position of the lipid phosphate groups in either leaflet. We then recorded the time evolution of the z coordinates of each of these water molecules throughout the trajectory frames. This data was then used to count the number of times water molecules entered the bilayer from one side, reached within 10 Å of the bilayer midplane, i.e. with $-10 \leq z \leq 10$ Å, and either moved through the opposite leaflet and exited from the other side (full transitions) or turned back and exited from the same side (partial transitions). The number of full and partial transitions was normalized by the lateral area of the bilayer and the total simulation time of the analyzed portion of the trajectory.

Defects were calculated with the PACKMEM tool [15] in 2 dimensions and with the algorithm from [16] in 3 dimensions as detailed in the SI.

To analyze the lipid and Chol diffusion from each trajectory, we first took the raw coordinates of the lipid phosphate atoms (P in CHARMM36 notation) or Chol's oxygen atom (O3 in CHARMM36 notation) from every trajectory frame output at a frequency of 20 ps, and unwrapped them (that is, removed any jumps in the coordinates between frames due to wrapping around the periodic boundaries). We then used the time evolution of these atoms' (x, y) positions to calculate the 2-dimensional mean squared displacement, $msd(t)$, and average it over all lipids (or all Chol molecules) in each leaflet. A small region of the $msd(t)$ function was then fit to $f(t) = 4Dt$ where D is the diffusion coefficient. This small region was chosen with a heuristic approach where consecutive 100-ns-long blocks of the $msd(t)$ function were fit to $g(t) = ax^b$ and the block with the largest b parameter was the one used for obtaining D. Representative plots of the data and fits is shown in Figure S14. Errors on the diffusion coefficients for each leaflet were calculated with a bootstrapping approach in which a dataset with the same total number of lipids was constructed by picking lipids at random, then the respective $msd(t)$ profiles were averaged and analyzed as above. The procedure was repeated multiple times and the standard deviation of the resulting diffusion coefficients was reported.

Further details can be found in the SI files.

Data availability
All data will be uploaded to a publicly accessible archive.

Code availability
All code used for analysis will be uploaded to a publicly accessible archive.

Methods References

1 Lorent, J. H. *et al.* Plasma membranes are asymmetric in lipid unsaturation, packing and protein shape. *Nat. Chem. Biol* **16**, 644-652 (2020). https://doi.org:10.1038/s41589-020-0529-6

2 Doktorova, M. *et al.* Preparation of asymmetric phospholipid vesicles for use as cell membrane models. *Nat. Protoc.* **13**, 2086-2101 (2018). https://doi.org:10.1038/s41596-018-0033-6

3 Ejsing, C. S. *et al.* Global analysis of the yeast lipidome by quantitative shotgun mass spectrometry. *Proc. Natl. Acad. Sci. U.S.A.* **106**, 2136-2141 (2009). https://doi.org:10.1073/pnas.0811700106

4 Buboltz, J. T. & Feigenson, G. W. A novel strategy for the preparation of liposomes: rapid solvent exchange. *Biochim. Biophys. Acta* **1417**, 232-245 (1999).

5 McIntosh, A. L. *et al.* Fluorescence and multiphoton imaging resolve unique structural forms of sterol in membranes of living cells. *The Journal of biological chemistry* **278**, 6384-6403 (2003). https://doi.org:10.1074/jbc.M205472200

6 Pinkwart, K. *et al.* Nanoscale dynamics of cholesterol in the cell membrane. *The Journal of biological chemistry* **294**, 12599-12609 (2019). https://doi.org:10.1074/jbc.RA119.009683

7 Lee, J. *et al.* CHARMM-GUI Membrane Builder for Complex Biological Membrane Simulations with Glycolipids and Lipoglycans. *J. Chem. Theory Comput.* **15**, 775-786 (2019). https://doi.org:10.1021/acs.jctc.8b01066
8 Abraham, M. J. *et al.* GROMACS: High performance molecular simulations through multi-level parallelism from laptops to supercomputers. *SoftwareX* **1**, 19-25 (2015).
9 de Jong, D. H. *et al.* Improved Parameters for the Martini Coarse-Grained Protein Force Field. *J. Chem. Theory Comput.* **9**, 687-697 (2013). https://doi.org:10.1021/ct300646g
10 Phillips, J. C. *et al.* Scalable molecular dynamics on CPU and GPU architectures with NAMD. *J Chem Phys* **153**, 044130 (2020). https://doi.org:10.1063/5.0014475
11 Yu, Y. *et al.* CHARMM36 Lipid Force Field with Explicit Treatment of Long-Range Dispersion: Parametrization and Validation for Phosphatidylethanolamine, Phosphatidylglycerol, and Ether Lipids. *J. Chem. Theory Comput.* **17**, 1581-1595 (2021). https://doi.org:10.1021/acs.jctc.0c01327
12 Fabian, B., Thallmair, S. & Hummer, G. Optimal Bond Constraint Topology for Molecular Dynamics Simulations of Cholesterol. *J. Chem. Theory Comput.* **19**, 1592-1601 (2023). https://doi.org:10.1021/acs.jctc.2c01032
13 Thallmair, S., Javanainen, M., Fabian, B., Martinez-Seara, H. & Marrink, S. J. Nonconverged Constraints Cause Artificial Temperature Gradients in Lipid Bilayer Simulations. *J. Phys. Chem. B* **125**, 9537-9546 (2021). https://doi.org:10.1021/acs.jpcb.1c03665
14 Doktorova, M. & Weinstein, H. Accurate in silico modeling of asymmetric bilayers based on biophysical principles. *Biophys. J.* **115**, 1638-1643 (2018). https://doi.org:https://doi.org/10.1016/j.bpj.2018.09.008
15 Gautier, R. *et al.* PackMem: A Versatile Tool to Compute and Visualize Interfacial Packing Defects in Lipid Bilayers. *Biophys. J.* **115**, 436-444 (2018). https://doi.org:10.1016/j.bpj.2018.06.025
16 Tripathy, M., Thangamani, S. & Srivastava, A. Three-Dimensional Packing Defects in Lipid Membrane as a Function of Membrane Order. *J. Chem. Theory Comput.* **16**, 7800-7816 (2020). https://doi.org:10.1021/acs.jctc.0c00609

Acknowledgments
We thank Madhusmita Tripathy and Anand Srivastava for providing their code for calculating packing defects in three dimensions, and Anne Kenworthy, Robert Ernst, and Itay Budin for critical reading of the manuscript. M.D. was supported by NIH F32GM134704. J.S. is funded by the Marie Skłodowska-Curie Actions Postdoctoral Fellowship (Grant 101059180). E.S. is funded by Karolinska Institutet, SciLifeLab, Swedish Research Council Starting Grant 2020-02682 and Human Frontier Science Program (Grant RGP0025/2022). F.A.H. is supported by NIH/NIGMS R01GM138887. E.L. was supported by R01 GM120351. J.L.S was supported by GM008280. K.R.L. and I.L. are supported by NIH (GM120351, GM134949), the Volkswagen Foundation (grant 93091), and the Human Frontiers Science Program (RGP0059/2019).

Author Contributions
M.D., K.R.L. and I.L. designed the research. J.L., E.L., E.S. and F.A.H. contributed ideas and expertise. M.D., J.L.S., X.Z., H.W., J.S. and K.R.L. performed and analyzed the experiments with cells and synthetic liposomes. E.L. and M.D. performed the molecular dynamics simulations and M.D. analyzed the simulation trajectories. M.D., K.R.L. and I.L. wrote the manuscript. All authors revised and edited the manuscript.

Competing Interest Declaration
The authors declare no competing interests.

Additional Information
Supplementary Information is available for this paper.

Correspondence and requests for materials should be addressed to Ilya Levental, Milka Doktorova and Kandice R. Levental.